

Design of detector to monitor the Bragg peak location of carbon ions by means of prompt γ -ray measurements with Geant4

Yan Fan¹ · Guang-Ming Huang¹ · Xiang-Ming Sun¹ · Zhen Wang¹ ·
Shu-Guang Zou¹ · Jun Liu¹ · Dong Wang¹ · Hui-Li Kang¹ · Ping Yang¹ ·
Hua Pei¹ · Da-Ming Sun¹ · Zi-Li Li¹

Received: 10 June 2017 / Revised: 27 July 2017 / Accepted: 16 August 2017 / Published online: 13 March 2018
© Shanghai Institute of Applied Physics, Chinese Academy of Sciences, Chinese Nuclear Society, Science Press China and Springer Nature Singapore Pte Ltd. 2018

Abstract Real-time monitoring of the Bragg peak location of carbon ions is urgently required for the quality control of hadron therapy. In this study, we design an annular detector to monitor the Bragg peak location of carbon ions with Geant4 simulation. This 360° surrounding structure has a high detection efficiency for the small-dose situation. The detector consists of a multilayered collimator system and an NaI scintillator for prompt gamma counting. The multilayered collimator includes a lead layer to prevent unwanted gammas and the paraffin and boron carbide layers to moderate and capture fast neutrons. An inclination of the detector further diminishes the background signal caused by neutrons. The detector, with optimized parameters, is applicable to carbon ions of different energies. In addition, the scintillator is replaced by an improved EJ301 organic liquid scintillator to discriminate gammas and neutrons. Inserting thin Fe slices into the liquid scintillator improves the energy deposition efficiency. The Bragg peak location of 200 MeV/u carbon ions can be monitored by prompt gamma detection with the improved liquid scintillator.

Keywords Bragg peak · Carbon ion · Prompt γ -ray · Geant4

1 Introduction

In recent years, cancer treatment based on hadron therapy has produced promising clinical results. Hadron therapy consists of treating cancerous tumors with proton or light ion beams (such as carbon ions) [1]. Clinical experience in carbon ion therapy has been accumulated for more than 10 years in Japan and Germany with extremely positive results, and hadron therapy developments are currently planned worldwide [2, 3]. The real-time monitoring of the Bragg peak location of protons or carbon ions is highly desirable for the quality control of hadron therapy. To monitor the location, gammas emitted from nuclear reactions must be detected, and two types of gammas can be used: coincident gammas from the production of positron emission isotopes, which are used in Positron emission tomography (PET) and prompt gammas from the excitations of the target nuclei by the ion or proton bombardment. In addition to PET, prompt γ -ray imaging appears as a good candidate to provide real-time information about the local dose both for proton [4, 5] and carbon ion [6] therapy.

To monitor the Bragg peak location of carbon ions, Min et al. used time-of-flight (TOF) technology to measure the prompt γ -ray [6–8]. Although neutrons are emitted preferentially at forward angles, its huge quantity in the transverse direction still causes considerable noise for the prompt gamma measurement [4]. The TOF setup can discriminate prompt photons from the neutron background. Using the TOF technology, a series of experiments was

This work was supported by the National Natural Science Foundation of China (Nos. 11375073 and U1232206).

✉ Yan Fan
fyanf@mails.ccnu.edu.cn
Guang-Ming Huang
gmhuang@phy.ccnu.edu.cn
Xiang-Ming Sun
xmsun@phy.ccnu.edu.cn

¹ PLAC, Key Laboratory of Quark & Lepton Physics (MOE), Department of Physics Science and Technology, Central China Normal University, Wuhan 430079, Hubei, China

performed at the GANIL (Caen, France) and GSI facilities, with 73, 95, and 305 MeV/u carbon ion beams [6–8]. However, the TOF technology requires a given phase of the RF-signal from the accelerator, which is affected by the beam time-structure [8]. In addition, it also requires a precise time setup to obtain the TOF spectrum, as well as avoiding the pile-up and dead-time effects. Therefore, the use of TOF introduces a challenge to the data acquisition (DAQ) system for the precise time detection requirements.

This paper focuses on the design of a detector with a multilayered shielding collimator system to reduce the time detection requirements. The detector is simulated with Geant4. In Sect. 2, we describe the physical models and packages used in the simulation. In Sect. 3, we analyze the energy and angular spectra of the secondary photons and neutrons that fly out of the water phantom. Section 4 describes the design of the NaI detector with a multilayered collimator system in detail. The optimized detector can monitor the Bragg peak location of 200 and 400 MeV/u carbon ions by prompt gamma counting at a spot of 10^6 . An improved EJ301 organic liquid scintillator detector is presented to replace the NaI scintillator with the same optimized collimator. With the suitable parameters, the Bragg peak of 200 MeV/u carbon ions can be detected by prompt gamma counting with its pulse shape discrimination ability.

2 Monte Carlo simulation tools configuration

The design study is based on Monte Carlo simulations with the code Geant4 version 4.9.6.p02. For the Standard model, this simulation used G4EmStandardPhysics_Option3, which is usually applied to medical physics simulation. In the Low Energy model [9], LowE_Penelope and LowE_Livermore are used. The Geant4 hadronic package [10] provides different models for elastic or inelastic scattering. We used G4HadronElastic for the elastic scattering process. Hadronic inelastic models include various phases of nuclear interactions: nuclear de-excitation, pre-equilibrium, intra-nuclear transport, and generator regime [11]. The package QGSP_BIC was applied to simulate these processes in our simulation, which was composed of QGS (quark gluon string model), PRECO (pre-compound model), and BIC (binary cascade model).

3 Secondary photons and neutrons

A box of water phantom with 40 cm length, 30 cm width, and 20 cm height was used for the simulation, because the human body is 70% water. A single spot of 10^6 200 MeV/u carbon ions was considered, because 10^6 – 10^7

ions are required to treat a 1 cm^3 tumor during one irradiation session, which delivers an equivalent dose of 1–2 Gy [12].

To find the appropriate parameters for the detector, the characteristics of secondary particles out of the phantom should be measured first. The quantity of the secondary particles is provided in Table 1. We have slightly more photons than neutrons: 16 photons and 10 neutrons per 100 incident carbon ions. Since the secondary particles are mainly photons and neutrons, the relative contributions of other particles can be neglected.

The energy and angular spectra of secondary photons and neutrons that left the water phantom are plotted in Fig. 1. Compared to the number of neutrons, the number of photons was much higher at $E < 10 \text{ MeV}$, but much lower at $E > 10 \text{ MeV}$. Neutrons are preferentially emitted at forward angles, whereas photons are mostly emitted at 90° – 120° . For generality, the case of 400 MeV/u carbon ions is also plotted in Fig. 1. For a single spot of 10^6 400 MeV/u carbon ions, an energy spectrum curve of secondary photons and neutrons is similar to that of 200 MeV/u carbon ions. In the angular spectrum, neutrons are emitted more forward within a cone of 10° , whereas photons are more concentrated at approximately 90° .

4 Design of the detector

When protons or carbon ions interact with the target matter, they deposit a maximum energy density in a region localized at the end of their path (the Bragg peak) [6]. The range of the beam in a medium is closely related to the distribution of the prompt gammas along the beam passage [6]. Prompt gamma counting is used to monitor the Bragg peak location of carbon ions by discriminating gammas and neutrons [6–8]. The optimal energy window is discussed to effectively discriminate the unwanted background gammas [13]. We seek to design a multilayered collimator system to suppress fast neutrons and to

Table 1 Simulated secondary particles that left the water phantom with 200 MeV/u carbon ions

Secondary particle	Quantity per carbon ion
Photon	0.164579
Neutron	0.099661
Proton	0.002686
e^+/e^-	0.006715
Others (deuteron, triton, ...)	0.002298

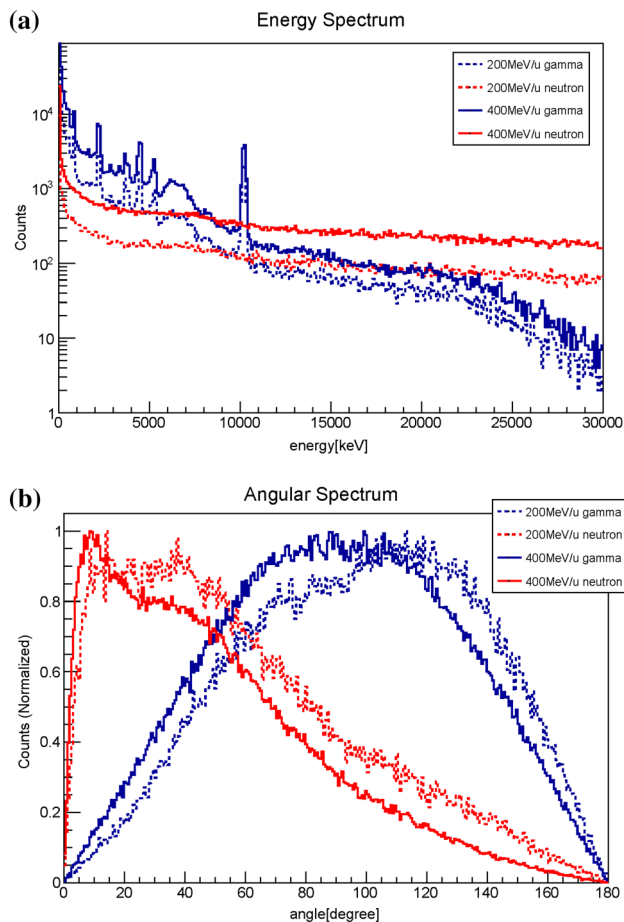


Fig. 1 (Color online) **a** Energy and **b** angular spectra of secondary photons and neutrons that left the water phantom

select the gammas that only pass the collimation slices. The details are discussed in the following sections.

4.1 Lead collimator to shield against unwanted gammas

Lead is often used to block the unwanted gammas, so we studied the parameters of the lead layer to obtain the Bragg peak location information from the secondary gammas. The components of the traditionally prompt gamma scanner (PGS) are shown in Fig. 2a: the collimator and detector are placed on the side perpendicular to the beam direction. The water phantom with 40 cm length (x -axis direction), 30 cm width (z -axis direction), and 20 cm height (y -axis direction) is set in the simulation. Here, the detector is designed as a cylinder-shape structure that completely surrounds the water phantom (360°), as shown in Fig. 2b. The collimator is considered as a cylinder structure, which consists of continuous alternating lead circle slices and air circle slices instead of the conventional lead block with apertures. The 100-mm-thick NaI scintillator is placed as

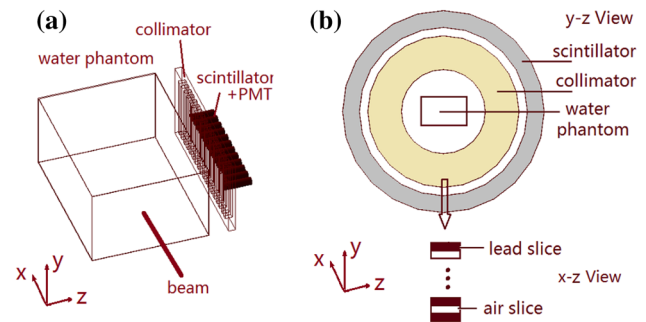


Fig. 2 (Color online) **a** Traditional collimator and detector geometry. **b** The designed detector in this simulation. The water phantom in **a**, **b** is identical

the outer ring. This geometry can improve the simulation efficiency by saving CPU time and memory cost and improving the detection efficiency in the measurement. It is useful to monitor the Bragg peak of carbon ions at small doses.

We directly obtain the characteristic parameters (spatial position, kinetic energy, and momentum direction) of each secondary gamma and neutron from the Geant4 program. Then, these secondary gammas with the established parameters are injected into the collimator and scintillator, and the statistics of the deposited energy and gamma counts in the NaI scintillator are obtained. In the simulation, the widths of the lead slice and air slice were set to 5 mm, and the thickness of the cylinder-shaped collimator was set to a variable value of 50–300 mm with the step value of 50 mm. Because the total longitudinal distance is 400 mm, the number of bins was set to 30 to obtain high accuracy. The bin width was reasonable for the HAMAMATSU PMT, whose diameter was 13 mm. Figure 3a shows the simulated distribution of gamma deposited energy in the scintillator for different collimator thicknesses in comparison to the 200 MeV/u carbon ion depth_dose profile in the water phantom (black bold line). The longitudinal position is the X -axis position, which is along the beam direction, as shown in Fig. 2. The gamma deposited energy curve is consistent with the Bragg peak location by suppressing unwanted gammas when the thickness of the lead collimator exceeded 150 mm. The downstream of the deposited energy falloff region significantly reduced with the increasing thickness of the collimator. Figure 3b indicates that the registered gamma counts in the detector have a similar curve and characteristics with the deposited energy. In other words, we can monitor the Bragg peak location of carbon ions by measuring the deposited energy or based on the count's statistics of prompt gammas. For simplicity, we only present the counts registered in the detector in the following sections.

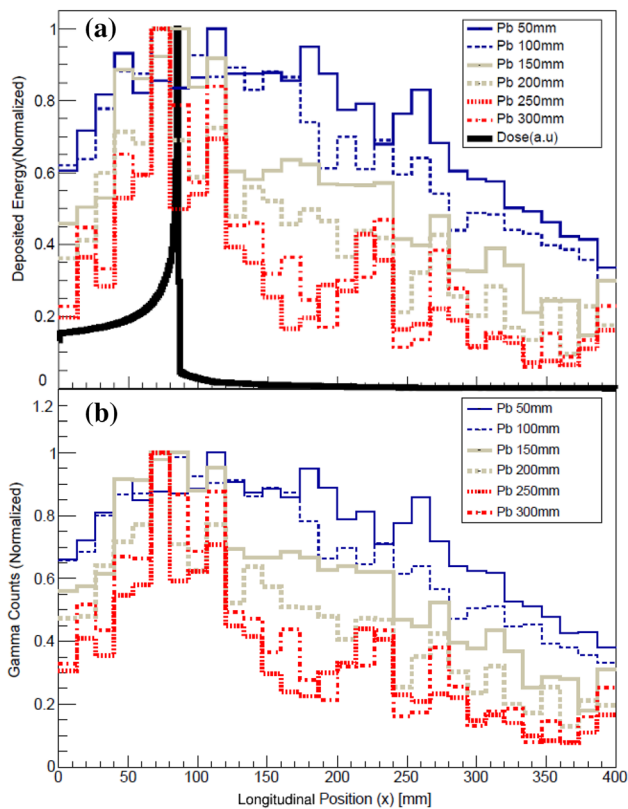


Fig. 3 (Color online) Simulated distribution of **a** the deposited energy and **b** counts of secondary gammas in the scintillator with different collimator thicknesses for a 200 MeV/u carbon ion beam. The dose (a.u) is the carbon ion theoretical depth_dose profile in the water phantom (black bold line)

Figure 4a plots the simulated counts detected in the scintillator with different settings for the collimator slice width when the thickness is fixed. When the collimator thickness is 200 mm, the detector can detect the Bragg peak location, as is demonstrated in Fig. 3. The gamma counts collected by the detector increase with the decrease in width of the lead slice. Thus, a higher detection efficiency requires a wider air slice and a thinner lead slice. Hence, the gamma counts with a 5-mm-wide lead slice (the first two cases in Fig. 4a) are larger than those with a 10-mm-wide lead slice (the latter two cases in Fig. 4a). Figure 4b shows the normalized counts detection with different air slice widths when the lead slice width is 5 mm. The wider air slice increases the number of unwanted gammas, so the 10-mm-wide air slice has more background counts than the 5-mm-wide one. Thus, the width of both air slice and lead slice should be set to 5 mm.

The process of the secondary gammas and neutrons injected to the detector is simulated with the following detector parameters: the collimator thickness is 200 mm, the slice width is 5 mm, and the NaI thickness is 100 mm. The counts received by the detector are shown in Fig. 5.

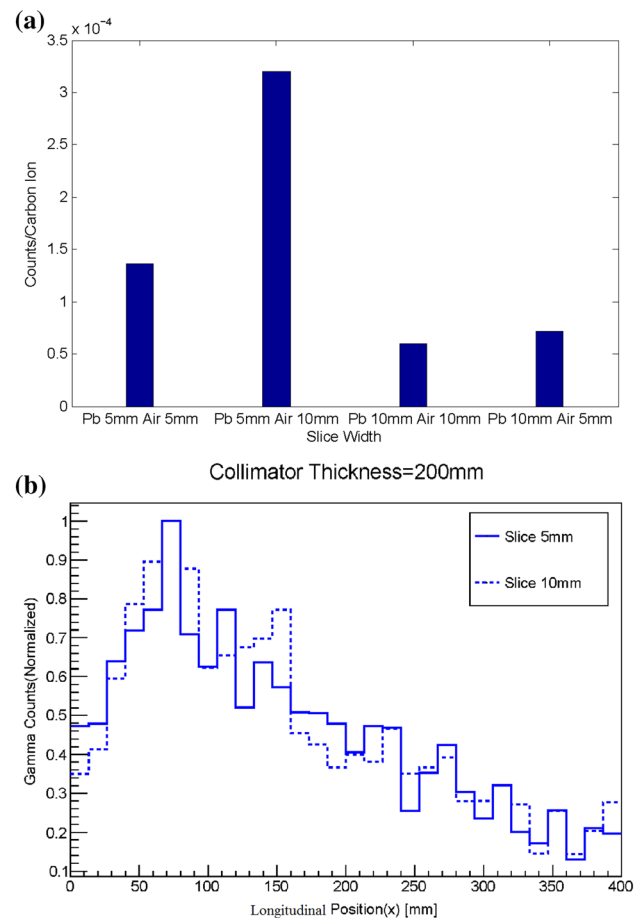


Fig. 4 (Color online) **a** Gamma counts at the Bragg peak location with different settings of collimator slice widths. **b** Registered gamma counts in the detector with different wide air slices (5-mm-wide lead slice, the first two cases in **a**)

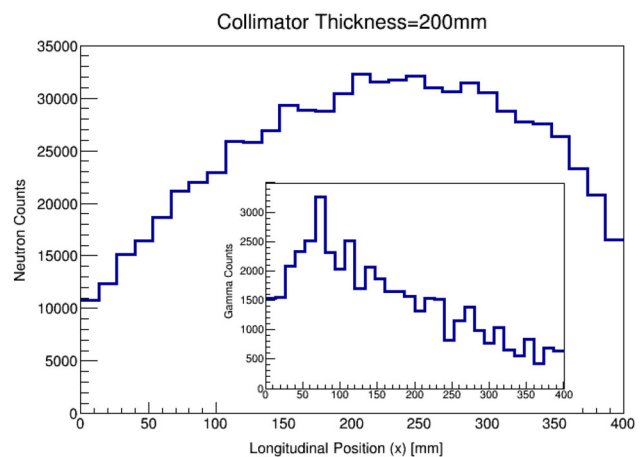


Fig. 5 (Color online) Counts registered in the detector of secondary gammas and neutrons

Figure 5 indicates that significantly more neutrons were detected in the scintillator than gammas because the lead could significantly shield against gammas, but had no

effect on the neutrons. Neutrons are highly forward-oriented, but sufficiently strong enough to compete with the signal collected at 90° if neutrons are not adequately shielded [4].

4.2 Shielding against the secondary neutrons by the paraffin layer and B_4C layer

Section 4.1 proved that the neutron counts in the scintillator are up to an order of magnitude larger than the received gamma counts. It is necessary to shield against these neutrons, which are generated from the water phantom.

Paraffin moderates the high-energy neutrons, and the boron carbide (B_4C) powder captures neutrons via the $B(n,\gamma)$ reaction, as demonstrated in Ref. [4]. We studied the shielding effect of the paraffin and B_4C on the mainly secondary particles that flew out of the water phantom.

First, gammas or neutrons with different kinetic energies are perpendicularly injected into a paraffin block, and the relationship of the deposited energy in the paraffin layer and the particle injection depth is shown in Fig. 6a, b. The energy deposition of neutrons is almost twice as much as that of gammas at the same injection depth, i.e., the shielding effect of the paraffin layer is more efficient on neutrons than on gammas, which is the result that we need. B_4C layer will further shields neutrons, so the collimator in Fig. 2b is replaced by a multilayered one. The paraffin and B_4C layers moderate and capture fast neutrons, and the lead layer prevents unwanted gammas. Figure 6c, d shows the counts of secondary gammas and neutrons, respectively, which flew out of the water phantom. Each figure shows the registered counts in the scintillator with different shielding layers. The effect of the shielding layers is significant, and the gamma counts with three shielding layers are approximately 1/6 of that with only the lead layer, whereas the neutron counts decreased by almost 90%.

The Bragg peak of the 200 MeV/u carbon ions in the water phantom is at approximately 80 mm, as indicated by the gamma counts profile in Fig. 6c. However, the neutron counts profile has a large counting behind the Bragg peak location, as shown in Fig. 6d, which is proven by experimental measurement in Ref. [7]. The method to eliminate this feature will be discussed in the following section.

4.3 Inclination of the detector

As shown in Fig. 1, the secondary neutrons that left the water phantom are emitted preferentially at forward angles. Thus, we inclined the detector to a certain angle to decrease the counts detected in the scintillator. The structure of the detector is shown in Fig. 7. Obviously, when the tilt angle a

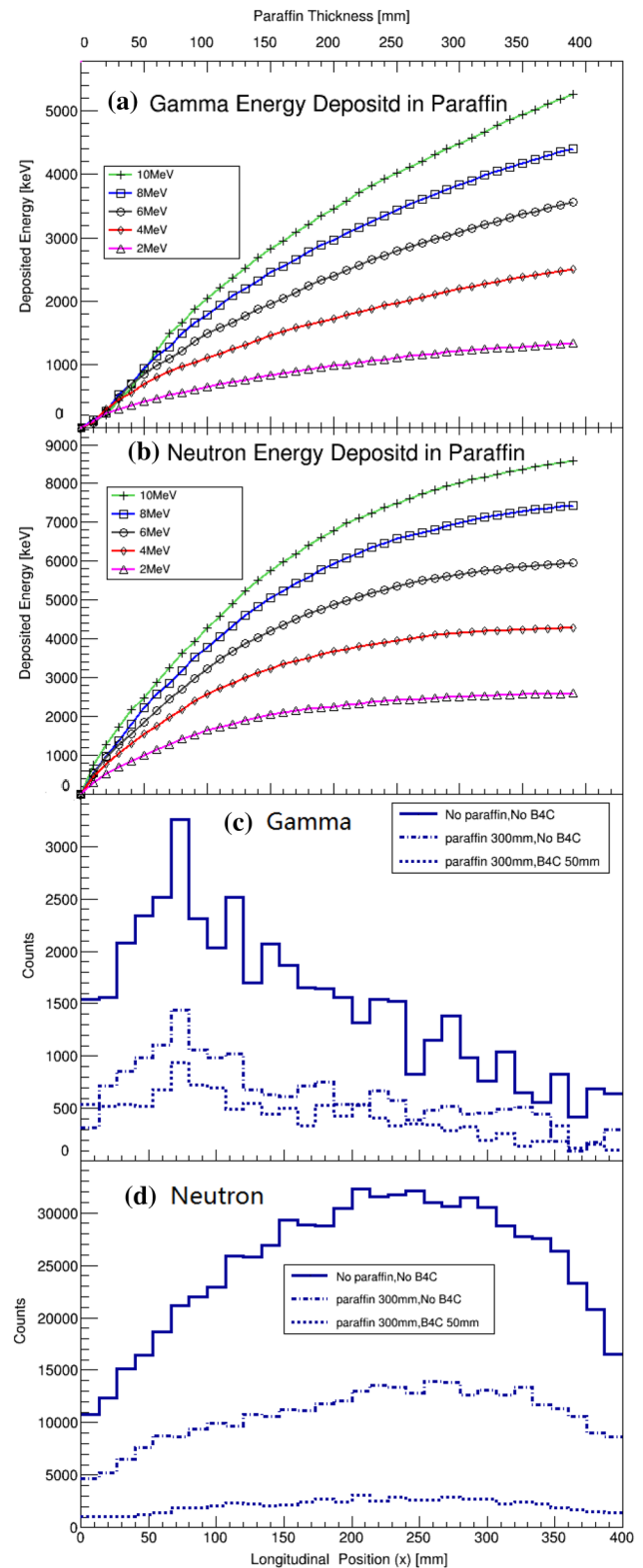


Fig. 6 (Color online) Energy deposition with the perpendicular **a** gamma and **b** neutron injection to the paraffin layer. The horizontal axis represents the thickness of the paraffin layer (above). **c** Gamma and **d** neutron counting in detector with different shielding layers. The horizontal axis represents the longitudinal position along the beam direction (below)

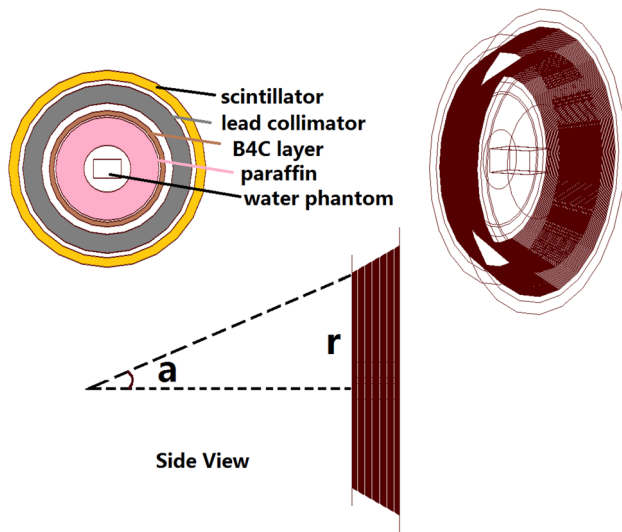


Fig. 7 (Color online) Inclination of the detector. Two important parameters: a is tilt angle of the detector; r is the distance between the central point in the water phantom and the start point of the detector

is set to zero, the detector in Fig. 7 becomes cylindrical, as discussed in the previous sections.

The registered counts in the detector with different tilt angles are shown in Fig. 8. Figure 8a, b shows the case of gammas and neutrons, respectively. The inclination of the

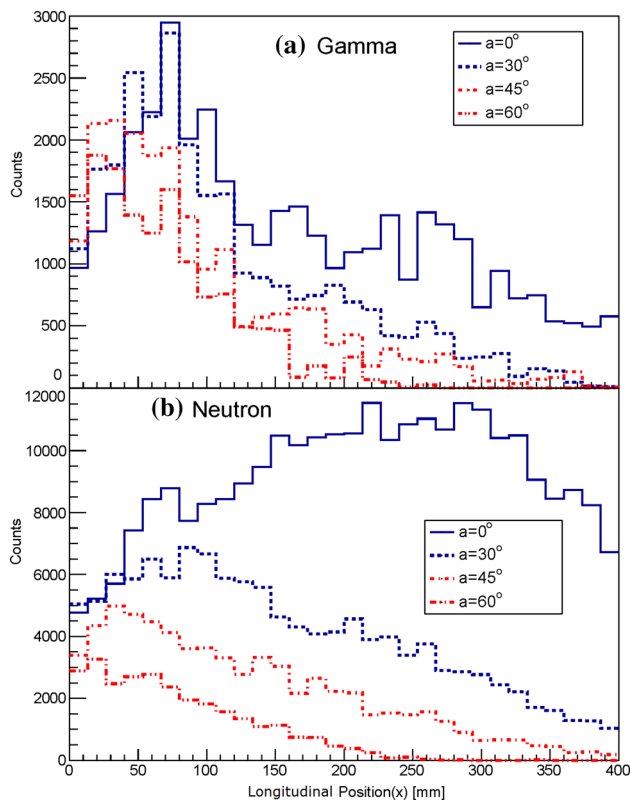


Fig. 8 (Color online) Registered counts of **a** gammas and **b** neutrons in the detector when the detector is placed with different tilt angles

detector significantly reduces the counts at the back of the longitudinal detection position. However, the counting curve peak shifts to the left with the increase in tilt angle a . To diminish this shift, parameter r , which is the distance between the central point in the water phantom and the start point of the detector, should increase; here, we set it to 700 mm, and angle a should decrease. If the tilt angle a is set to 30° , the peak of the gamma counts curve is only slightly affected, whereas the neutron counts were significantly suppressed at the back end of the longitudinal detection position.

4.4 Optimized parameters of detector

The effects of the paraffin and B_4C layers and the inclination of the detector are indicated in the above sections. Here, we discuss the optimized parameters for the detector (200 MeV/u $^{12}C^{6+}$ ion beam). Tilt angle a should be less than 30° , as demonstrated in Sect. 4.3. The lead layer should be 200 mm thick, and the lead slice and air slice should be 5 mm wide, as indicated in Sect. 4.1. The role of the paraffin layer is to moderate fast neutrons, so the shielding against neutrons slightly changes when the thickness exceeds 300 mm. The shielding effect of B_4C layer is discussed as follows, and the detector counting of secondary neutrons with different thicknesses of B_4C layer is shown in Table 2.

The result indicates that B_4C layer could capture the neutrons, and the effect improves with the increase in thickness of the layer. The shielding effect appears saturated with the continuous increase in the thickness of B_4C layer. Thus, B_4C layer should be 30 ~ 50 mm thick from an economical and practical viewpoint. The optimized parameters for the detector are shown in Table 3.

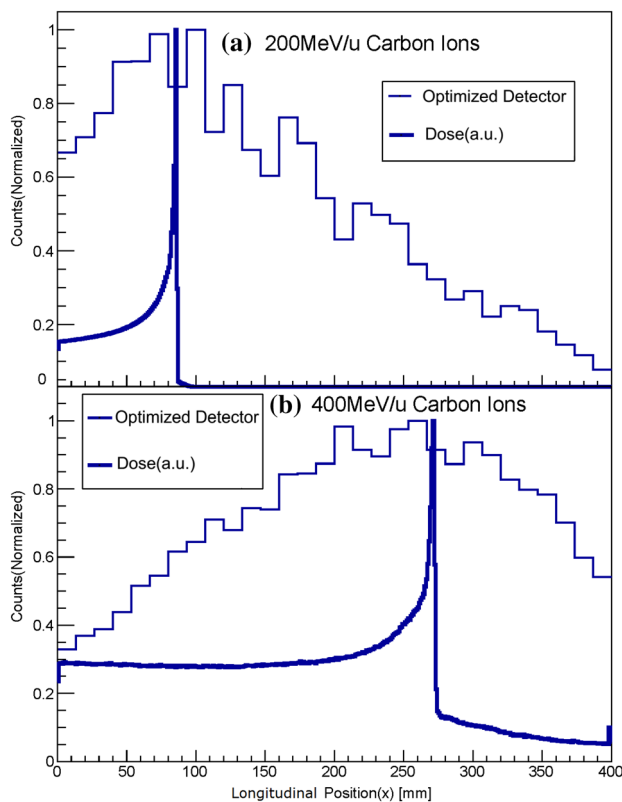
A single spot of 10^6 200 MeV/u carbon ions was injected into the water phantom. The detector with the optimized parameters in Table 3 was used for counting. The counts curve registered in the detector is illustrated in Fig. 9a in comparison with the theoretical dose falloff curve. Here, B_4C layer was 30 mm thick. The optimized

Table 2 Registered counts in the detector by neutrons with different thicknesses of B_4C layer

B_4C layer thickness (mm)	Counts/carbon ions
10	0.030728
30	0.027255
50	0.02546
60	0.025272
70	0.023982

Table 3 Optimized parameters for the detector

Parameters	Values
Angle a ($^\circ$)	30
Distance r (mm)	700
Lead slice width (mm)/air slice width (mm)	5/5
Paraffin layer thickness (mm)	300
B ₄ C layer thickness (mm)	30–50
Lead layer thickness (mm)	200
NaI thickness (mm)	100

**Fig. 9** (Color online) Counts detection of the **a** 200 MeV/u and **b** 400 MeV/u carbon ions with the optimized detector

detector could effectively detect the Bragg peak location by shielding against secondary neutrons effectively. A single spot of 10^6 400 MeV/u carbon ions was injected to the water phantom. Figure 1 shows that secondary neutrons emitted more in the forward direction with angles within 10° , so the tilt angle could be set to 0. Other parameters were identical to those in Table 3. The counting detection curve of the longitudinal position (x) for 400 MeV/u carbon ions is shown in Fig. 9b.

4.5 Improved EJ301 organic liquid scintillator detector

Section 4.4 demonstrated that the optimized detector can effectively work, but the counts of secondary neutrons still bring the background signal around the Bragg peak location. Thus, discriminating prompt photons from the neutron background would enable the real-time monitoring with prompt γ -rays. Here, the EJ301 liquid organic scintillator was considered another selection for the gamma counting because of its strong neutron/gamma pulse shape discrimination (PSD) ability [14]. Because the gamma response function of the EJ301 detector has been studied in Ref. [15], the EJ301 detector can also work for gamma counting. It is well known that the advantage of inorganic crystals over organic scintillators lies in their greater stopping power due to their higher density and larger atomic number (Z). Thus, as a liquid, low-density, low- Z organic scintillator, EJ301 has inevitably poor efficiency for gamma detection compared to the NaI scintillator. To increase the energy absolute efficiency, we inserted several thin slices of high Z material (Fe) into the liquid scintillator, as shown in Fig. 10. These Fe slices are just like cooling fins with identical thick gaps, as shown in the right side of Fig. 10. When these Fe slices were inserted into the EJ301 organic liquid scintillator (the left side of Fig. 10), the gaps were filled with liquid. When photons deposited energy in the Fe slice, electrons were produced. The electrons that escaped from the Fe slice deposited energy into the EJ301 liquid. In other words, the inserted Fe slices were used to increase the gamma deposited energy or counts instead of blocking gammas. With the fixed total thickness of the Fe slices and gap distance, different Fe slice thicknesses will cause different detection efficiencies. The Fe slice thickness and gap distance were set to identical values to obtain identical relative densities.

A single spot of 10^6 200 MeV/u carbon ions was injected into the water phantom. The deposited energies in different detectors are quoted in Table 4. All the detectors

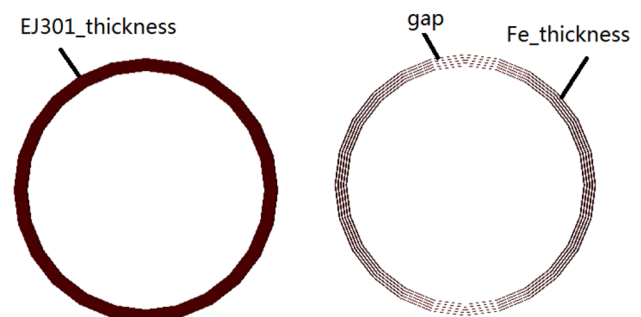
**Fig. 10** (Color online) Improved EJ301 organic liquid scintillator geometry

Table 4 Deposited energy in the optimized NaI detector and EJ301 detector

Detector	Deposited energy/ions (keV)
NaI	2.456358
Common EJ301	0.8158864
EJ301 with 100 μm slice	1.6213327
EJ301 with 200 μm slice	1.581599
EJ301 with 250 μm slice	1.2865053

had the identical parameters shown in Table 3, but the scintillator was NaI or EJ301. The thickness of these scintillators was 200 mm. The last three lines of Table 4 show the improved EJ301 detector with different thicknesses of Fe slices. The common EJ301 detector has a much lower energy deposition efficiency than the NaI detector. However, the improved EJ301 detector with inserted Fe slices achieves higher energy deposition efficiency than the common EJ301 detector without Fe slices. Furthermore, the deposited energy increases with the decrease in thickness of the Fe slice. The feasible reason may be that a thinner the slice enables more electrons to escape, and more energy will deposit in EJ301.

The deposited photon energy and the gamma counts registered in the improved EJ301 detectors with different kinds of Fe slice thicknesses are plotted in Fig. 11. The Bragg peak of 200 MeV/u carbon ions was not detected in the case of 100- μm -thick Fe slices possibly because too many elastic collisions would damage the Bragg peak location information. When the Fe slice was 200 or 250 μm thick, the improved EJ301 organic liquid scintillator detector could monitor the Bragg peak location. We only discuss the counts caused by secondary gamma for the improved EJ301 detector. Other performance indicators, such as the neutron detection efficiency and data acquisition (DAQ) system, may be further investigated in the future.

5 Discussion and conclusion

PET is currently the commercial clinical method for in vivo and in situ monitoring in charged particle therapy. In recent years, many research achievements have been made in PET studies by simulation or testing [16–18]. A PET detector module that combines the depth-of-interaction (DOI) and TOF capabilities has achieved good energy resolution and reasonable time resolution [17]. Thus, it has promising application perspectives in clinical PET systems. However, the main

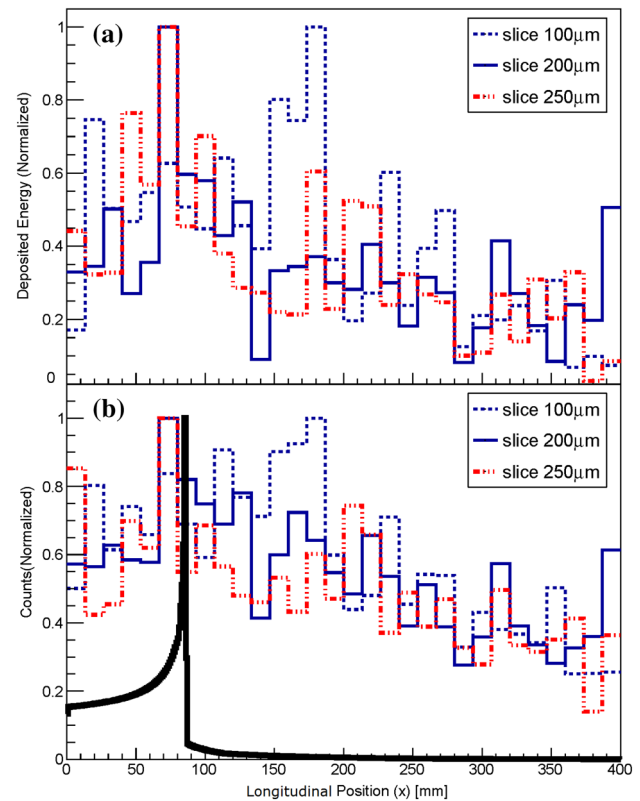


Fig. 11 (Color online) Simulated distribution of secondary gammas **a** deposited energy, and **b** counts in scintillator with different kinds of collimator thickness for the 200 MeV/u carbon ion beam

drawback of PET imaging for particle therapy is the low β^+ activity induced by fragmentation.

A conceptually similar method to the PET range verification idea is the use of prompt gamma radiation. Prompt gammas result in a much higher counting rate at production, which may enable the range verification at a relatively low dose delivery, and there is no biological washout. Thus, we designed a ring detector to monitor the Bragg peak location of carbon ions via prompt gammas counting with Geant4 simulation. Because the discrimination of prompt gammas from background radiation is important to prompt photon radiation, an inclined NaI detector with a multilayered collimator system is proposed here. With the optimized parameters, the Bragg peak location of 200 and 400 MeV/u carbon ions can be detected at a spot of 10^6 .

In addition, an improved EJ301 organic liquid scintillator detector is proposed for gamma counting detection instead of the NaI scintillator. Several Fe slices are inserted into the liquid scintillator to improve the energy absorption efficiency. Nevertheless, the improved EJ301 scintillator has a lower energy detection efficiency than the NaI scintillator. Furthermore, a lower efficiency implies fewer reaction instances, which results in a significantly poorer energy resolution. This behavior is not beneficial to the

measurement of the Bragg peak location. Nevertheless, because of the good PSD ability, we can discriminate the prompt gammas from the background signals (mainly secondary neutrons). In this simulation, the improved EJ301 detector can monitor the Bragg peak location of 200 MeV/u carbon ions with a suitable slice thickness based on either gamma deposited energy or gamma counting, as demonstrated in Fig. 11. Thus, the effect of the energy resolution on the measurement is not so important. The improved EJ301 detector is a candidate, in addition to the NaI detector.

In conclusion, we used Geant4 to simulate an optimized detector with a multilayered collimator system. The optimized detector could monitor the Bragg peak of carbon ions at a relatively low dose (a spot of 10^6). The scintillator in the optimized detector is preferably NaI, and the improved EJ301 scintillator is also a viable option.

References

- G. Kraft, Tumortherapy with ion beams. *Nucl. Instrum. Meth. A* **454**, 1–10 (2000). [https://doi.org/10.1016/S0168-9002\(00\)00802-0](https://doi.org/10.1016/S0168-9002(00)00802-0)
- U. Amaldi, G. Kraft, Radiotherapy with beams of carbon ions. *Rep. Prog. Phys.* **68**, 1861–1882 (2005). <https://doi.org/10.1088/0034-4885/68/8/R04>
- G. Kraft, Ion beam therapy in Europe, Application of Accelerators in Research and Industry: Twentieth International Conference. *AIP Conference Proceedings*, **1099**, 429–434 (2009). <https://doi.org/10.1063/1.3120066>
- C.H. Min, C.H. Kim, M.Y. Youn et al., Prompt gamma measurements for locating the dose falloff region in the proton therapy. *Appl. Phys. Lett.* **89**, 183517 (2006). <https://doi.org/10.1063/1.2378561>
- J.C. Polff, S. Peterson, M. McCleskey et al., Measurement and calculation of characteristic prompt gamma ray spectra during proton irradiation. *Phys. Med. Biol.* **54**, 519–527 (2009). <https://doi.org/10.1088/0031-9155/54/22/N02>
- E. Testa, M. Bajard, M. Chevallier et al., Monitoring the Bragg peak location of 73 MeV/u carbon ions by means of prompt gamma-ray measurements. *Appl. Phys. Lett.* **93**, 093506 (2008). <https://doi.org/10.1063/1.2975841>
- E. Testa, M. Bajard, M. Chevallier et al., Dose profile monitoring with carbon ions by means of prompt-gamma measurements. *Nucl. Instrum. Meth. B* **267**, 993–996 (2009). <https://doi.org/10.1016/j.nimb.2009.02.031>
- E. Testa, M. Bajard, M. Chevallier et al., Real-time monitoring of the Bragg-peak position in ion therapy by means of single photon detection. *Radiat. Environ. Biophys.* **49**, 337–343 (2010). <https://doi.org/10.1007/s00411-010-0276-2>
- S. Chauvie, S. Guatelli, V. Ivanchenko, et al., Geant4 Low Energy Electromagnetic Physics, in Conference Record 2004 IEEE Nuclear Science Symposium, **3**, 1881–1885 (2004). <https://doi.org/10.1109/NSSMIC.2004.1462612>
- J.P. Wellisch, Hadronic shower models in Geant4—the frameworks. *Comput. Phys. Commun.* **140**, 65–75 (2001). [https://doi.org/10.1016/S0010-4655\(01\)00256-9](https://doi.org/10.1016/S0010-4655(01)00256-9)
- G.A.P. Cirrone, G. Cuttone, F. D. Rosa, et al., Validation of Geant4 Physics Models for the Simulation of the Proton Bragg Peak, in Conference Record 2006 IEEE Nuclear Science Symposium, **N22-2**, 788–792 (2006). <https://doi.org/10.1109/NSSMIC.2006.355969>
- D. Schardt, Tumor therapy with high-energy carbon ion beams. *Nucl. Phys. A* **787**, 633–641 (2007). <https://doi.org/10.1016/j.nuclphysa.2006.12.097>
- C.H. Min, J.G. Park, S.H. An et al., Determination of optimal energy window for measurement of prompt gammas from proton beam by Monte Carlo simulations. *J. Nucl. Sci. Technol.* **45**, 28–31 (2014). <https://doi.org/10.1080/00223131.2008.10875777>
- L. Chang, Y. Liu, D. Long et al., Pulse shape discrimination and energy calibration of EJ301 liquid scintillation detector. *Nucl. Tech.* **38**, 1–6 (2015). <https://doi.org/10.11889/j.0253-3219.2015.hjs.38.020501>. (in Chinese)
- S.Y.L.T. Zhang, Z.Q. Chen, R. Han, Study on gamma response function of EJ301 organic liquid scintillator with GEANT4 and FLUKA. *Chin. Phys. C* **37**, 126003 (2013). <https://doi.org/10.1088/1674-1137/37/12/126003>
- J. Wu, Y.Q. Liu, T.Y. Ma et al., GATE simulation based feasibility studies of in-beam PET monitoring in ^{12}C beam cancer therapy. *Nucl. Sci. Technol.* **21**, 275–280 (2010). <https://doi.org/10.13538/j.1001-8042/nst.21.275-280>
- Q.Y. Wei, T.P. Xu, T.T. Dai et al., Development of a compact DOI-TOF detector module for high-performance PET systems. *Nucl. Sci. Technol.* **28**, 43 (2017). <https://doi.org/10.1007/s41365-017-0202-2>
- M.A. Piliero, N. Belcari, M.G. Bisogni et al., First results of the INSIDE in-beam PET scanner for the on-line monitoring of particle therapy treatments. *J. Instrum.* **11**, C12011 (2016). <https://doi.org/10.1088/1748-0221/11/12/C12011>